Journal of Alloys and Compounds 973 (2024) 172910

Contents lists available at ScienceDirect

Journal of Alloys and Compounds

journal homepage: www.elsevier.com/locate/jalcom

Vanadium-induced structural effects on the corrosion and tribological properties of an Al-Li binary alloy

Augustine Nana Sekyi Appiah [a,*], Anna Woźniak [a], Przemysław Snopiński [b,*], Krzysztof Matus [a], Paweł M. Nuckowski [a], Gilmar Ferreira Batalha [c], Shuhratjon Abdugulomovich Nazarov [d], Izatullo Navruzovich Ganiev [e], Marcin Adamiak [a,*]

[a] Materials Research Laboratory, Faculty of Mechanical Engineering, Silesian University of Technology, 18A Konarskiego Street, 44-100 Gliwice, Poland
[b] Department of Engineering Materials and Biomaterials, Silesian University of Technology, 18A Konarskiego Street, 44-100 Gliwice, Poland
[c] Department of Mechatronics and Mechanical Systems Engineering, Polytechnic School of Engineering of the University of Sao Paulo (USP), São Paulo 05508-900, Brazil
[d] Department of Machinery and Devices, Engineering and Technological Faculty, Technological University of Tajikistan, Dushanbe 734061, Tajikistan
[e] Nikitin Institute of Chemistry, National Academy of Sciences of Tajikistan, Dushanbe 734063, Tajikistan

ARTICLE INFO

Keywords:
Lightweight alloys
Grain refinement
EBSD analysis
Wear rate
Microstructure
Phase evolution
Corrosion current density

ABSTRACT

The influence of vanadium transition metal alloying on the structure, corrosion resistance and tribological properties of a binary Al-Li alloy containing 6 wt % Li was investigated in this research. Varying vanadium contents of 0.05 wt %, 0.1 wt %, 0.5 wt %, and 1.0 wt % were examined. The results demonstrate that the addition of 1.0 wt % vanadium optimally enhanced the corrosion resistance and wear resistance of the alloy. With 1.0 wt % V, the wear rate decreased from $3.6 \pm 0.50 \times 10^{-2}$ m^3/m to $1.5 \pm 0.07 \times 10^{-2}$ m^3/m, the hardness increased from 51.7 ± 7.3 HV to 77.6 ± 4.1 HV, and the corrosion current density decreased from 43.6 $\mu A/cm^2$ to 3.9 $\mu A/cm^2$. Microstructural analyses revealed significant grain refinement induced by the addition of vanadium. The grain size decreased by 36.7 %, and the dendrite arm spacing (DAS) decreased from 35 μm to 8 μm. Adding vanadium reduced the overall porosity of the alloy resulting from a peritectic reaction leading to the formation of vacancy-solute complexes at the grain boundaries. Phase and chemical composition analyses confirmed the formation and presence of δ (AlLi) strengthening phase within the interdendritic regions, particularly with the addition of 1.0 wt % V. The presence of this phase strongly contributed to the observed improvements in corrosion resistance and tribological properties of the vanadium-modified alloy.

1. Introduction

Aluminum and its alloys have gained widespread utilization across various industries owing to their unique properties, including low density, excellent corrosion resistance, and good formability. The versatility of aluminum-based materials has rendered them indispensable in sectors spanning from automotive to aerospace. However, to meet the escalating demands for materials that are simultaneously lightweight and robust, researchers have persistently endeavored to enhance the performance of aluminum alloys through post-processing treatments [1–3] as well as optimization of production conditions [4]. A notable advancement in aluminum alloy technology is the development and utilization of aluminum-lithium (Al-Li) alloys.

Lithium, being the lightest metallic element with an atomic mass of approximately 7 g/mol, a solid density of 0.534 g/cm^3 at 20 °C, a body-centered cubic (BCC) crystal structure, and a melting temperature of 181 °C, offers exceptional prospects for alloying with aluminum. Elemental aluminum, possessing a face-centered cubic (FCC) crystal structure and a solid density of 2.7 g/cm^3 at 20 °C, has been reported in literature to be significantly improved in terms of properties by incorporating lithium. Each 1 % increase in lithium content in an Al-Li alloy corresponds to a reduction in density by approximately 3 % and an increase in stiffness by approximately 5 % [5].

The utilization of Al-Li alloys presents numerous advantages compared to traditional aluminum alloys such as the series 2000 and 5000, which have copper and manganese as the main alloying elements, respectively. These encompass lower densities, higher elastic moduli, excellent fatigue and cryogenic strength, as well as improved toughness

* Corresponding authors.
E-mail addresses: augustine.appiah@polsl.pl (A.N.S. Appiah), przemyslaw.snopinski@polsl.pl (P. Snopiński), marcin.adamiak@polsl.pl (M. Adamiak).

https://doi.org/10.1016/j.jallcom.2023.172910
Received 6 September 2023; Received in revised form 12 November 2023; Accepted 17 November 2023
Available online 20 November 2023

properties and resistance to crack growth. However, it has been observed that the resistance to crack growth in these alloys is influenced by a jagged crack path that induces roughness-induced crack closure under tension-dominated loading [6]. Crack closure diminishes the severity of stress intensity at the crack tip when subjected to an external load, rendering it beneficial [7]. Unfortunately, certain loading conditions involving compressive overloads flatten the crack surfaces, resulting in reduced or eliminated crack closure and a significant acceleration in crack growth rates [8]. Consequently, Al-Li alloys become vulnerable to corrosion and wear failure, posing a substantial challenge [9].

To address these challenges, intensive research have focused on post-casting and post-processing heat treatment methods to enhance the mechanical properties of Al-Li alloys [10,11]. These studies have reported that achieving high strength in Al-Li alloys typically involves precipitation heat treatments similar to those employed for conventional Al-alloys, albeit with certain variations. Peak strength in many Al-Li alloys is attained through a combination of precipitation heat treatment and prior cold work (stretching) or the inclusion of ancillary key alloying elements such as zirconium (Zr) to control grain microstructure during heat treatment [12,13].

Despite these advancements, heat treatment operations in Al-Li alloys suffer from siginificant drawbacks. Desirable heat-treated conditions often result in highly anisotropic mechanical properties, characterized by reduced ductility and fracture toughness in the short transverse direction [14,15]. Moreover, microstructurally short cracks exhibit rapid growth rates, enabling swift crack initiation and potentially leading to early cracking in high-stress regions such as rivet holes [6,16]. These limitations undermine the alloy's resistance to corrosion and tribological properties, which are crucial properties considering their applications in the aerospace industry for structural components in airframes, aerospace vehicle skins, and spacecraft fuel tanks.

The production of aluminum-lithium alloys has undergone significant advancements, particularly with the emergence of the third generation Al-Li alloys in the 1990 s. These alloys, featuring lithium contents ranging from 1 wt % to 2 wt %, have gained unparalleled popularity and widespread adoption in the aerospace industry due to their remarkable versatility in various applications. However, when it comes to specific uses such as seat tracks, door rails, flying control structures, stiffeners, and floor installations in aircrafts like the EH101 helicopter, the demand for Al-Li alloys with lithium contents exceeding 2 wt %, such as alloy AA8090, has risen to replace alloys AA7075, AA7010, and AA2024 [17]. In this regard, recent research studies [18–20] have been devoted to exploring ways of enhancing the mechanical properties of Al-Li alloys containing more than 2 wt % lithium, employing post-processing techniques or alloying with other metals to achieve remarkable property enhancements.

Vanadium, a highly versatile transition metal, is extensively utilized as an alloying constituent in a wide range of materials, including steel, aluminum alloys, and titanium alloys. Its distinct properties and promising potential for applications in materials engineering make it a subject of significant interest and investigation. A comprehensive understanding of the Al-V binary system [21] provides valuable insights into the formation of various compounds, namely $Al_{21}V_2$, $Al_{45}V_7$, $Al_{23}V_4$, Al_3V, and Al_9V_5. These compounds emerge through peritectic reactions at temperatures: 670 ºC, 688 ºC, 736 ºC, 1360 ºC, and 1670 ºC, respectively. Under conditions of temperatures exceeding 1500 ºC and pressures beyond 3 GPa, the precipitation of the AlV phase containing the AlV_3 intermetallic compound occurs. This compound exhibits a hexagonal structure with parameters a = 0.7070 nm and c = 0.9565 nm. Notably, at lower temperatures below 1500 ºC, AlV_3 takes on a metastable phase characterized by a tetragonal structure with parameters a = 0.6167 nm and c = 0.9481 nm. These compounds and phases formed by the incorporation of V in Al contribute to improving the properties of the alloy. In a study conducted by Sahli et al. [22], the focus was on investigating the impact of Vanadium (V) addition to the A6061 aluminum alloy, processed using the accumulative roll bonding method (ARB). The researchers found that by adding 0.1 or 0.2 wt % V to the A6061 ARBed alloy, they achieved a notable enhancement in both ductility and strength, leading to a 22 % increase in resistance compared to the ARBed A6061 without vanadium addition. Although there was a slight reduction in elongation due to detachments at the interfaces, the overall improvements were attributed to the combined effects of segregation and solid solution strengthening caused by V addition. Furthermore, vanadium has shown remarkable effects in enhancing the corrosion resistance of aluminum alloys by promoting the formation of protective oxide films, thereby reducing corrosion rates [23]. These distinctive properties of vanadium position it as an effective transition metal for enhancing the mechanical properties of lightweight metal alloys.

The objective of this research is to explore a pathway to enhancing the corrosion resistance and tribological properties of Al-Li alloys prior to post-casting heat treatments. The novelty lies in using two subsequent approaches. Firstly, we aim to develop an Al-Li alloy with a lithium content of 6 wt %. Recent studies [24–26] have indicated that lithium contents ranging from 5.0 wt % to 10.3 wt % in light metals such as magnesium and aluminum are optimal for achieving exceptional strength while reducing weight. Secondly, we will incorporate vanadium as an alloying element and investigate the effects of different vanadium concentrations on the corrosion resistance and tribological properties of the cast alloys. To gain a comprehensive understanding of the vanadium-induced property enhancements, the casting process will be followed by potentiodynamic corrosion resistance tests, tribological tests, and the samples will undergo characterization using techniques including scanning electron microscopy (SEM), optical microscopy, electron backscatter diffraction (EBSD), x-ray diffraction (XRD), energy-dispersive x-ray spectroscopy (EDS), Archimedes density tests and Vickers microhardness tests.

2. Methodology

2.1. Sample preparation

The alloys used in this study were fabricated through the combination of aluminum grade A995 (GOST 110669–74), lithium-LE1 (GOST 8774–75), and vanadium grade VnPl-1 (99.94 %). The alloys were synthesized within corundum crucibles, using a resistance furnace, SShOL (mine experimental laboratory resistance). The temperature of the furnace was set to a range of 750–850 °C. To initiate the synthesis, an aluminum-vanadium master alloy was utilized as a precursor material, which was placed beneath a layer of a flux mixture comprising NaCl-35 + KCl-35 + LiF-30 %. The precise amount of vanadium was calculated and then carefully introduced into the preheated aluminum melt at a temperature of 750 °C. Once introduced, the components were thoroughly mixed, and any slag present on the surface of the melt was removed. Subsequently, lithium (with a weight percentage of 6.1 %) was added to the melt, in a form encased in aluminum foil. To facilitate the incorporation of lithium, a bell-shaped device was employed. This allowed for efficient stirring of the melt until complete dissolution of the lithium took place. Following this step, the slag was removed once more to ensure a purified composition. Cylindrical specimens, featuring diameters ranging from 8 to 10 mm and lengths between 60 and 100 mm,

Table 1
Prepared Al-Li alloy specimens used for this study.

Sample designation	As-cast composition
B	Al+ 6 %Li
V1	Al+ 6 %Li + 0.05 wt % V
V2	Al+ 6 %Li + 0.1 wt % V
V3	Al+ 6 %Li + 0.5 wt % V
V4	Al+ 6 %Li + 1.0 wt % V

were cast from the resulting melt using a graphite mold. Table 1 outlines the specimens prepared for this study, which comprised compositions of Al+ 6 %Li, varying in vanadium content.

The metallographic samples for examination were prepared using an automated grinding and polishing system. The specimens underwent a comprehensive metallographic preparation process, involving grinding using SiC papers, polishing with a coarse diamond suspension, and achieving a mirror-like finish using 0.04 μm colloidal silica. Subsequently, the polished surfaces were etched using Keller's reagent. This reagent consists of nitric acid (2.5 vol %), hydrochloric acid (1.5 vol %), hydrofluoric acid (1.0 vol %), and distilled water.

2.2. Corrosion test

Pitting corrosion resistance was tested using the potentiodynamic method by recording anodic polarization curves. The test stand comprised of Atlas 0531 EU potentiostat (ATALS-SOLLICH, Rębiechowo Poland) and a typical three-electrode system. An Ag/AgCl electrode was used as the reference electrode. The auxiliary electrode was a platinum electrode of the PtP-201 type. The corrosion tests started after 3600 s of open-circuit potential stabilization (E_{ocp}). Next, the anodic polarization curves were recorded taking measurements from the potential using Eq. (1) at a scan rate of 0.375 mV s^{-1}.

$$E_{start} = E_{ocp} - 100mV \tag{1}$$

The corrosion tests were carried out in 3.5 % sodium chloride aqueous solution at room temperature. A 3.5 % NaCl solution was applied due to its widespread usage for the corrosion tests of aluminium alloys. Similar test conditions for lightweight metals, including aluminium based alloys have been used in studies by Babilas et al. [27] and Yan et al. [28].

2.3. Wear test

Wear resistance experiments were performed employing the CSM tribometer (CSM Instruments, Switzerland) using the ball-on-plate method in a dry sliding environment. Cylindrical Al-Li specimens, 10 mm in diameter, were employed as the test samples, while a 316 stainless steel ball, 6 mm in diameter, served as the opposing specimen. The maximum contact pressure was determined using the Hertzian contact theory [29] for spherical counter-samples and planar samples, as expressed by Eq. (2).

$$P_{\max} = \frac{3F}{2\pi a^2} \tag{2}$$

Where: P_{max} is maximum contact pressure (GPa), F is normal load (N), and a is contact radius (mm) - calculated according to Eq. (3).

$$a = \sqrt[3]{\frac{\frac{3F}{8}\cdot\left(\frac{1-\vartheta_1^2}{E_1}\right)+\left(\frac{1-\vartheta_2^2}{E_2}\right)}{\frac{1}{d_1}+\frac{1}{d_2}}} \tag{3}$$

Where: ϑ is Poisson's ratio, E is Young's modulus (GPa), d is diameter of curvature (mm), and designations $_1$ – tested samples (Al-Li alloy) and $_2$ – counter samples ball. The Young's modulus of Al-Li alloy containing 6 at % lithium is 75–77 GPa [30], and the Poisson ratio for commercial Al-Li alloy (e.g. 8090Al-Li) is 0.33 [31]. However, it is found that each 1 % increase in lithium content in an Al-Li alloy corresponds to a decrease in the Poisson ratio by 3 %. Based on this, for the calculation, the Poisson ratio of Al-6 %Li alloy was set at 0.30. The Young`s modulus and Poisson ratio of 316 L stainless steel (counter sample) were 190 GPa and 0.28 respectively. The diameter of the stainless-steel ball was 6 mm, and the surface of the tested samples was unlimited (flat surface – top surface of cylindrical samples with 10 mm diameter). The wear test was carried out using a normal load Fn of 3 N, which corresponds to the maximum Hertzian pressure (contact stress) of approximately 600 MPa. Similar value of the maximum Hertzian pressure during wear test of aluminum based alloy were used by Zhang et al. [32]. The ultimate tensile strength of commercial Al-Li alloys lies in the range of 490 (8090 alloy) to 550 MPa (20291 alloy). The addition of vanadium to Al-Li alloys results in enchanced mechanical properties [33]. The selected test conditions allow for the evaluation of the influence of vanadium concentration in aluminum-lithium-based alloys on the wear behavior and the performance of measurements under critical force conditions. The stroke length was 5 mm and the frequency 2.5 Hz creating a sliding speed of 4 cm/s. The tests were performed in atmospheric conditions at a relative humidity of 50 – 60 % at ambient temperature. Based on the performed measurements, the value of the coefficient of friction (COF) was determined. Prior to the test, samples and counter samples were cleaned using ethanol. The test of each sample was performed three times, to ensure consistency and reproducibility. Images of the depth of the wear tracks were taken using 3D visualization with Leica 3D microscope DVM6 (Leica Microsystem, Wetzlar, Germany).

2.4. Density and hardness tests

The density and volume of the investigated specimen were measured by employing the Archimedes method using the laboratory analytical balance Radwag AS310/X (Radwag, Radom, Poland). The specimens' metallographic cross-sectional Vicker's hardness was assessed using the FM-ARS 9000 hardness tester (Future Tech Corporation, Tokyo, Japan) with a 4.9 N load. To measure microhardness, the XY cross-sections of the samples were prepared through metallographic polishing. Each sample underwent 100 measurements, covering a 2.0 mm × 2.0 mm area. The measurements were conducted in a 10 × 10 matrix pattern, with a consistent horizontal and vertical displacement of 0.20 mm between each measurement.

2.5. Microstructure and phase characterization

The microstructure examinations involved the utilization of different analytical techniques. Light microscopy and AxioVision software from ZEISS, Jena, Germany were employed, along with scanning electron microscopy (SEM) using a Zeiss Evo MA 15 series instrument equipped with an X-ray energy dispersive spectrometry (EDS) system. Electron backscatter diffraction (EBSD) was utilized in the SEM at an operating voltage of 20 kV and a step size of 0.2 μm to characterize grain size and crystallography.

For phase analysis, X-ray diffraction was conducted using a PANalytical X'Pert Pro diffraction system from Panalytical B.V. (currently: Malvern Panalytical Ltd.), Almelo, The Netherlands. A cobalt anode lamp (KαCo λ = 0.179 nm) was used, operating at a voltage of 40 kV with a filament current intensity of 30 mA. The measurements were performed in the Bragg–Brentano geometry, covering an angular range of 20 – 110° 2θ with a step size of 0.05° and a step count time of 100 s. The resulting diffractograms were analyzed using the X'Pert High Score Plus software (v. 3.0e) with the dedicated Inorganic Crystal Structure Database-ICSD (FIZ, Karlsruhe, Germany).

3. Results

3.1. Corrosion and tribological properties

The open circuit potential (E_{ocp}) curves recorded over time are depicted in Fig. 1(a), while Fig. 1(b) illustrates Tafel plots for the tested samples. Regarding the base sample (B) under initial conditions, the E_{ocp} value initially increased and then shifted towards more electropositive values. After approximately 3350 s, the E_{ocp} value abruptly dropped from −623 to −741 mV vs. Ag/AgCl. Such sudden changes in E_{ocp} values indicate alterations in the rates of the anodic and/or cathodic processes. This variation in E_{ocp} values is attributed to the instability of the

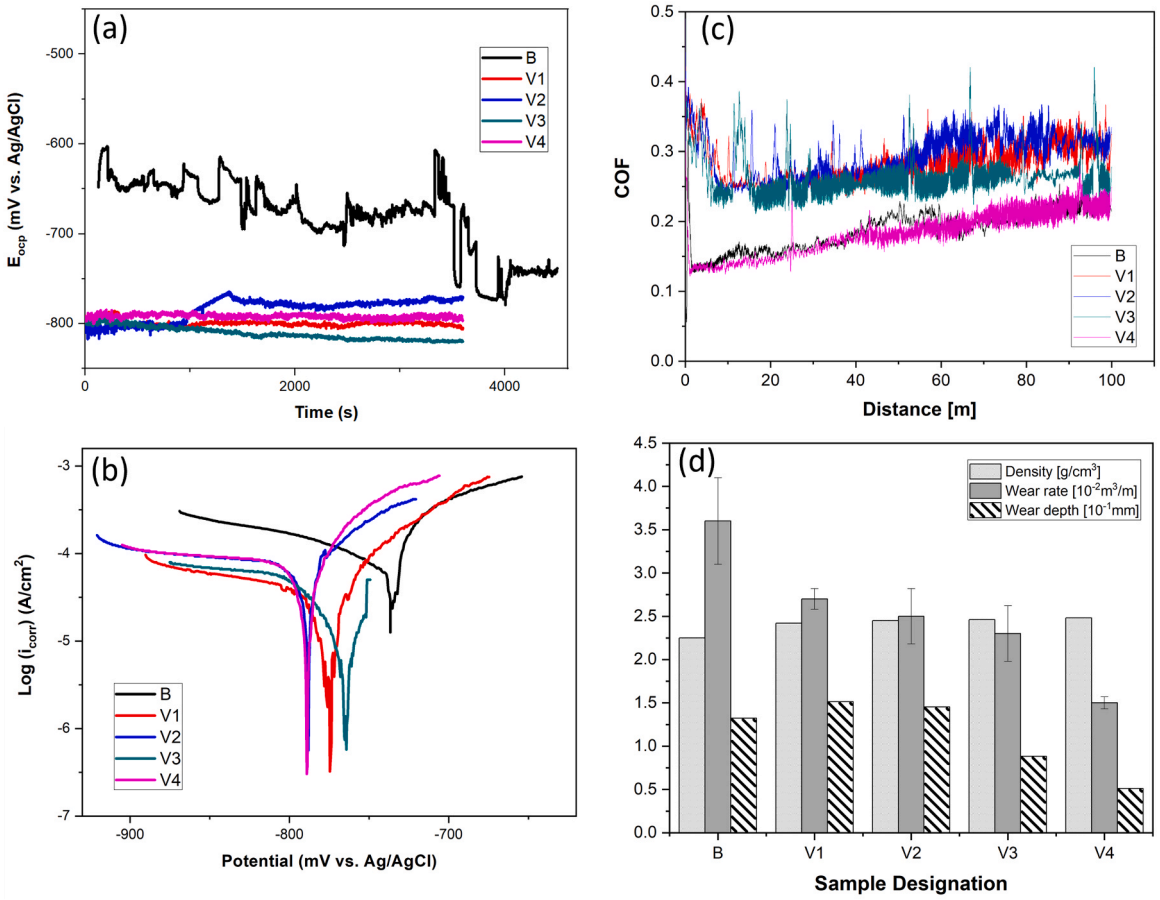

Fig. 1. Results of corrosion and tribology studies: (a) E_{ocp} changes as a function of time, (b) Anodic polarization curves for tested samples, (c) Wear coefficient (COF) as a function of wear distance and (d) Comparative column chart showing the density, wear rate and wear depth of investigated samples.

electrochemical activity of the formed oxide film or localized corrosion on the metal surface in the aqueous solution. The final E_{ocp} values for the base Al-6 %Li correspond to that registered for 2196 Al-Li alloy presented by Chen et. al. [34]. For samples V1-V4, which have been alloyed with vanadium, the E_{ocp} potential exhibited minimal changes over time. The highest open circuit potential value was observed for the base material (sample B), with a mean value of Eocp = −759 mV vs. Ag/AgCl. In contrast, the E_{ocp} values for the samples with varying concentrations of vanadium were similar, ranging from −794 to −781 mV vs. Ag/AgCl. The corrosion potentials determined from Tafel plots in Fig. 1(b) aligned with the open circuit potential values in Fig. 1(a). The corrosion potential (E_{corr}) for the base material was −736 mV vs. Ag/AgCl, which represented the noblest value among the tested group. Upon addition of 0.05 wt %V, the recorded E_{corr} was −814 mV vs. Ag/AgCl. Similar values were recorded for all specimens containing Vanadium, as −785 mV vs. Ag/AgCl, −776 mV vs. Ag/AgCl, and −810 mV vs. Ag/AgCl for specimens containing 0.1 wt %V, 0.5 wt %V and 1.0 wt %V respectively.

However, despite the favorable E_{corr} of the Al-6 %Li base alloy, the corrosion current density (i_{corr}) was high at i_{corr} = 43.6 μA/cm^2. It was discovered that incorporating vanadium into the chemical composition of Al-Li alloys led to lower corrosion current densities and, consequently, improved corrosion behavior. The i_{corr} values for samples V1, V2 and V3 were 11.7 μA/cm^2, 12.2 μA/cm^2 and 13.8 μA/cm^2 respectively, which were nearly four times lower than that of the base material. Furthermore, the lowest i_{corr} value was recorded for sample V4, with 1 % weight concentration of vanadium, with a mean value of i_{corr} = 3.9 μA/cm^2. The positive impact of vanadium addition on the corrosion behavior of Al-based alloys has also been reported by Esteves et al. [35] and Ozdemir et al. [23]. They stipulated that the enhanced corrosion resistance of samples with vanadium can be attributed to a decrease in the concentration and mobility of point defects resulting from the incorporation of vanadium into the passive layer.

The evolution of the wear coefficient or coefficient of friction (COF) for all tested samples is depicted in Fig. 1(c). Throughout the wear resistance test, a consistent trend of COF reduction was observed initially for all tested samples. This phenomenon can be attributed to the point contact between the test sample and the counter-sample, resulting in elevated local compressive pressures and subsequent high shear stress. As a consequence, the contacting surface underwent sequential deformation and fragmentation, leading to accelerated wear. Consequently, the contact area between the frictional couple increased over time, leading to a decrease in pressure and a gradual reduction in wear rate. For samples B, V1, and V2, an increase in COF was observed. However, it is noteworthy that the V3 and V4 samples exhibited a distinct behavior. After reaching 38 m of sliding distance, their COF values remained stable, measuring 0.26 and 0.22, respectively. These values represent the lowest COF measurements among all the tested samples.

The density, wear rates, and depth of wear of the samples are presented and compared in Fig. 1(d). The base Al-6 %Li alloy exhibited a density of 2.25 g/cm^3, as determined by employing the Archimedes principle at room temperature. Upon the addition of 0.05 wt % vanadium in sample V1, the density increased to 2.42 g/cm^3. Subsequent additions of vanadium resulted in marginal density increments, yielding 2.45 g/cm^3, 2.46 g/cm^3, and 2.48 g/cm^3 for samples V2, V3, and V4, respectively. Notably, the base alloy's density showed a 12 % increase upon alloying with 1 wt % vanadium (V4). This observation however

suggests that the V4 alloy possesses remarkable lightweight characteristics compared to commercially available Al-Li alloys currently employed in aerospace applications. These alloys, as reported in literature typically exhibit densities ranging from 2.63 g/cm^3 to 2.88 g/cm^3 [36,37].

The wear rate, Q (in m^3/m) was calculated using Eq. (4), where Ls (m) is the sliding distance, and Vs (in m^3) is the volume loss. According to the Archard law, Vs is inversely proportional to the hardness, H, and was computed using Eq. (5), where W is the applied load and k is the wear coefficient.

$$Q = \frac{V_s}{L_s} \tag{4}$$

$$V_s = \frac{kWL_s}{H} \tag{5}$$

The plot in Fig. 1**(d)** reveals the wear rate exhibited its tested peak value in the base alloy, specifically at $Q = 3.6 \pm 0.50 \times 10^{-2}$ m^3/m. Subsequently, this rate demonstrated a consistent decrease as small amounts of vanadium were added, reaching its minimum in the alloy containing 1 wt % vanadium with a value of $Q = 1.5 \pm 0.07 \times 10^{-2}$ m^3/m. The wear depth measured for the tested specimens is also depicted and compared in Fig. 1(d), and detailed depth maps, obtained from 3D visualization are presented in supplementary Fig. S1. Analyses of wear depth revealed penetration of the tribology tester to a depth of 132 μm from the tested surface in the base Al-6 %Li. The depth further increased to 151 μm after alloying with 0.05 wt %V. However, there was an observed reduction in the depth of wear to 145 μm after alloying with 0.1 wt %V and further reduction to 88 μm upon addition of 0.5 wt %V. The lowest depth of penetration was recorded for the specimen containing 1.0 wt %V at 51 μm, representing approximately 160 % reduction in the depth of penetration. These declines in wear rate and wear depth signify a substantial enhancement in wear resistance following the introduction of 1 wt % vanadium into the alloy.

In order to comprehend the disparities in corrosion and wear characteristics between the base and vanadium-modified alloys, a deeper exploration of their underlying mechanisms was undertaken. Pitting corrosion emerged as the primary mode of corrosion in all test samples. Fig. 2 displays SEM images illustrating the corrosion pit morphologies for the base material (Fig. 2(a)) and the alloy modified with 1 wt % vanadium (Fig. 2(b)). Notably, the base material exhibited larger and deeper pits, with an approximate diameter of 138 μm, while the 1 wt % vanadium-modified alloy had relatively shallower and smaller pits, measuring around 56 μm in diameter. These findings substantiate the observed disparity in corrosion resistance, with the base material demonstrating the lowest corrosion resistance and the 1 wt % vanadium-modified alloy exhibiting the highest. To gain insights into the elemental composition within these corrosion pits, Energy Dispersive X-ray Spectroscopy (EDS) was employed. Fig. 2 and Table 2 provide EDS spectra and chemical compositions for the corrosion pits in the base material (B_{corr}) and the 1 wt % vanadium-modified alloy (V_{corr}). Notably, EDS revealed the presence of oxygen, which contributes to the formation of passivating oxides, elements sodium (Na) and chlorine (Cl), which originate from the NaCl solution used in the corrosion tests as well as iron (Fe).

Pitting corrosion in aluminum-based alloys typically originates at the interface between iron-rich regions and the alloy matrix. According to existing literature [38], it has been observed that these iron-rich areas serve as cathodic sites, creating an alkaline environment around them and leading to localized dissolution of the passive film. Subsequently, the rapid oxidation of aluminum, triggered by the interaction between the Al-based alloy and the corrosive environment, initiates pitting corrosion. Frankel [39] has noted that the formation of localized acidity within the pit results from the hydrolysis of metal cations. The introduction of vanadium into the aluminum-based alloy has two notable effects [40]: 1. It impedes the maintenance of a critical pit solution necessary for pit growth, thereby reducing the dissolution rate. 2. It releases corrosion inhibitors in the form of vanadates, which are oxidized vanadium species. Based on our observations from SEM and EDS investigations, and corroborated by data from recent studies [41], it can be concluded that achieving a uniform dispersion of alloying elements, such as vanadium, and depositing them onto iron-rich regions can promote the repassivation of pits during the early stages of corrosion.

Fig. 3 presents the wear tracks observed after tribology testing. The base alloy, depicted in Fig. 3(a), exhibits prominent deep ploughing

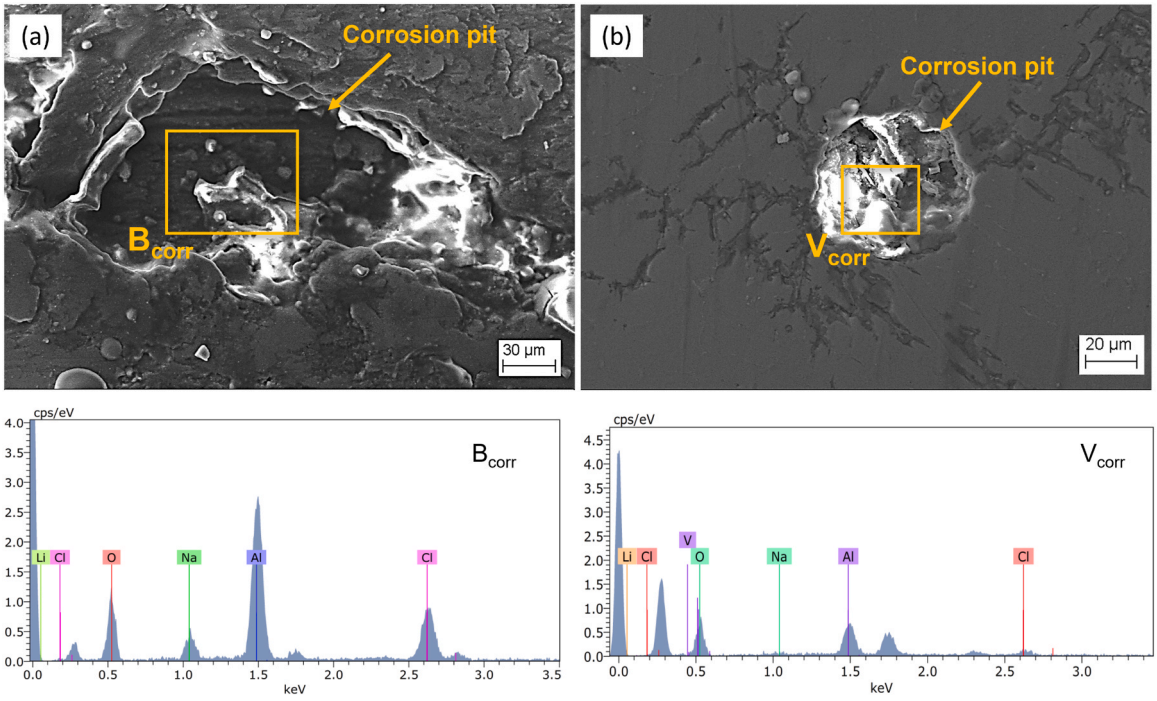

Fig. 2. Morphology and chemical composition of corrosion pits (a) Base material (b) alloy modified with 1 wt % vanadium (V4).

Table 2
chemical composition of corrosion pits.

	Concentration	Li	O	Na	Al	Cl	Fe	V
B_{corr}	Weight %	88.73	1.08	–	29.13	0.06	0.25	–
V_{corr}	Weight %	62.77	4.22	0.05	32.42	0.03	0.10	0.61

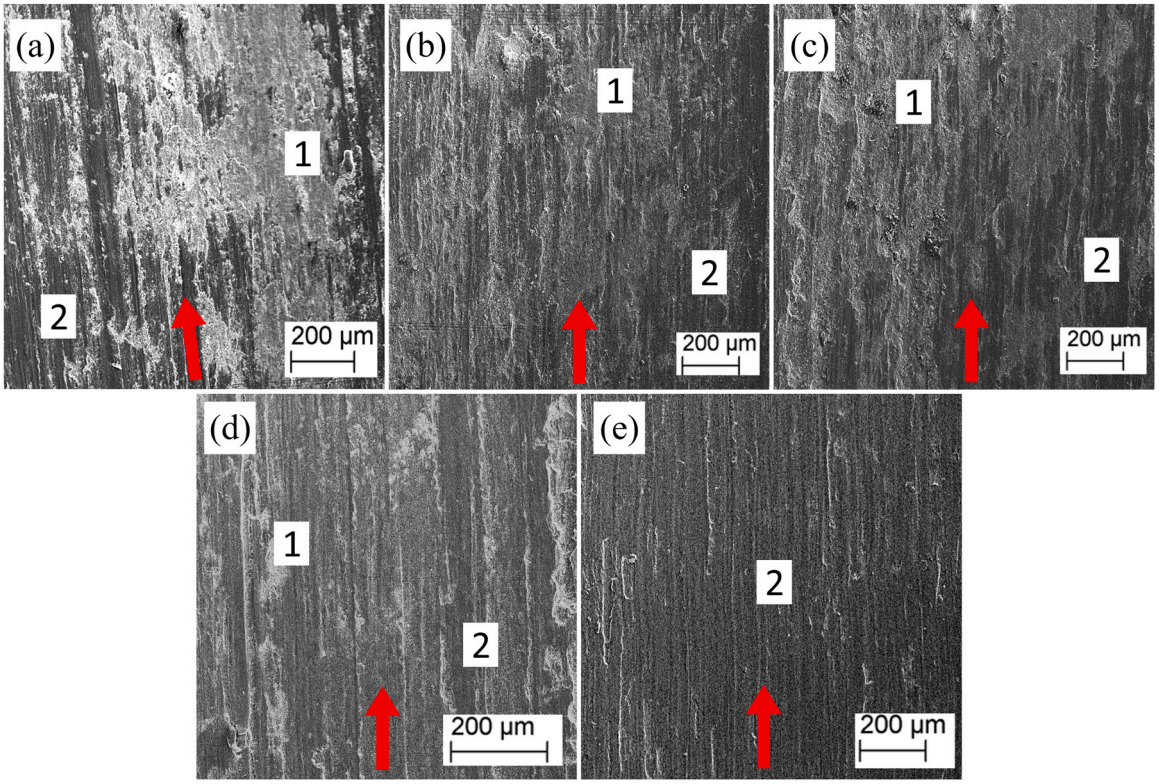

Fig. 3. Wear morphology of samples after tribology testing showing 1. Delamination wear, and 2. Abrasive grooves (a) sample B, (b) sample V1, (c) sample V2, (d) sample V3, and (e) sample V4.

grooves that contribute to the delamination of the surface layer. Conversely, the wear tracks of the vanadium-containing samples (Fig. 3 (b-e)) display shallower delaminating features, which correspond to the lower observed wear rates. Although delamination was also observed in the vanadium-alloyed samples, its occurrence decreased as the concentration of vanadium increased. Notably, at 1 wt % vanadium, delamination was minimal and mostly negligible. These observations suggest that the wear mechanism observed in the tested specimens is a combination of delamination wear (region 1) and abrasive wear (region 2). The findings derived from the tribology tests indicate that specimens exhibiting larger volumes of delamination wear also experience higher wear rates in comparison to those with lower occurrences of delamination. This highlights the significance of delamination and abrasive wear as contributing factors to overall wear in the investigated specimens.

3.1.1. Hardness

Vickers microhardness measurements were systematically conducted to comprehensively evaluate the mechanical performance of the investigated alloys subsequent to the incorporation of varying concentrations of vanadium. The experimental analysis involved subjecting the polished samples to rigorous testing, taking 100 measurements along the through-thickness cross-section of each specimen, and the results are presented in Fig. 4. The base alloy exhibited a relatively lower hardness value, measured at 51.7 ± 7.3 HV, in comparison to the other investigated samples. However, with the strategic addition of the vanadium alloying element, a remarkable enhancement in hardness was observed, particularly evident when the alloy contained 1 wt % vanadium. In this scenario, the hardness soared to 77.6 ± 4.1 HV, denoting a significant increase of approximately 50 % compared to the vanadium-free alloy counterpart.

3.1.2. Porosity

The porosity of each specimen (∅) was quantified using Eq. (6).

$$\varnothing = \frac{V_V}{V_T} \times 100 \tag{6}$$

Where V_V represents the volume of voids in the specimen, and V_T denotes the total volume of the specimen. The base Al-6 %Li alloy (Fig. 5 (a)) exhibited a porosity of 11.71 %, with the largest pore having a diameter of 193.79 µm. The specimen containing 0.05 wt %V (Fig. 5(b)) demonstrated a reduction in porosity, measuring 10.72 %, and the largest pore diameter was 39.28 µm. A slight decline in porosity to 10.63 % was observed for sample V2, containing 0.1 wt %V (Fig. 5(c)), with the largest pore diameter at 65.92 µm. Subsequently, further incorporation of 0.5 wt %V in sample V3 (Fig. 5(d)) led to a porosity of 10.60 %, and the largest pore measured 58.37 µm. The least porosity among the investigated specimens was recorded for the specimen containing 1.0 wt %V (Fig. 5(e)), with a porosity of 9.90 % and a measured diameter of 45.46 µm for the largest pore.

Fig. 5(f) provides a comparative summary of the porosities in the investigated specimens, revealing an approximate 18 % decrease in

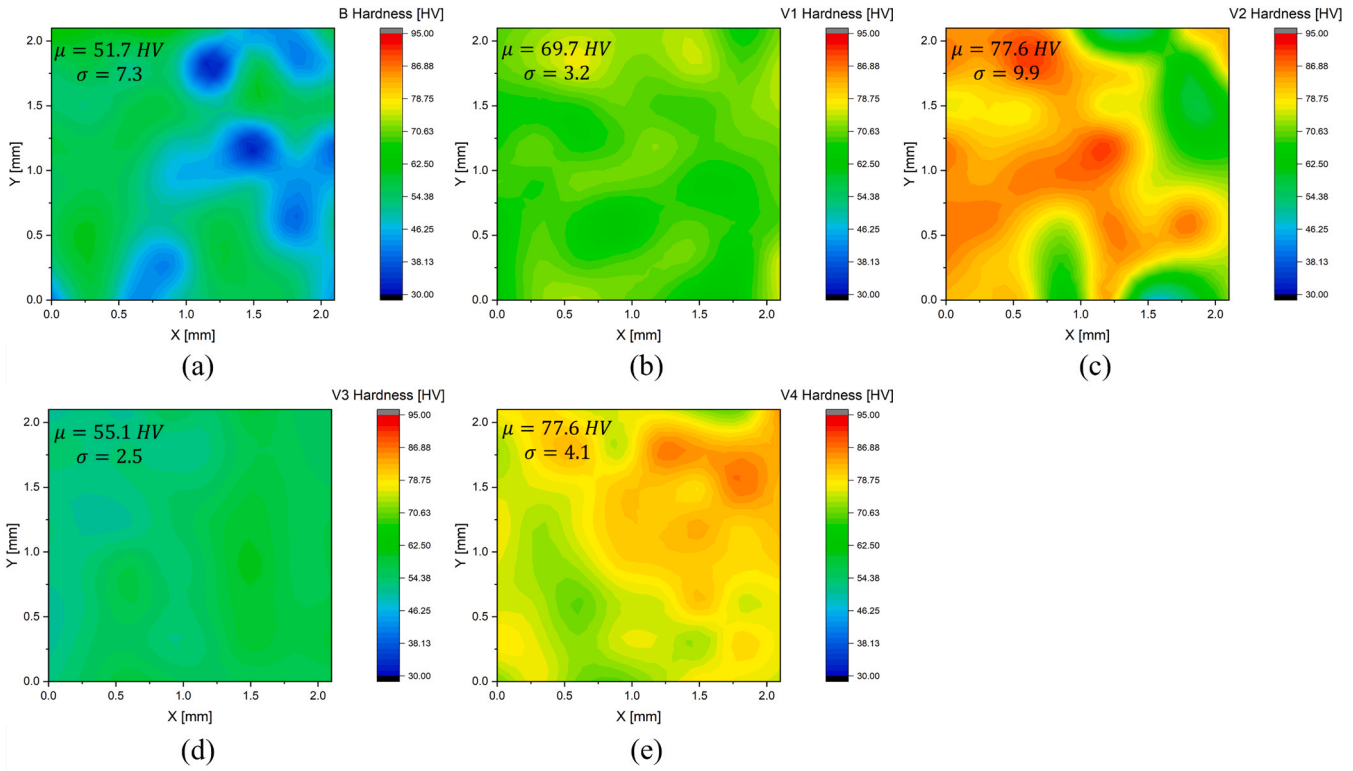

Fig. 4. Vicker's microhardness maps of investigated samples with the microhardness mean (μ) and standard deviation (σ) (a-e) samples B, V1, V2, V3 and V4, respectively.

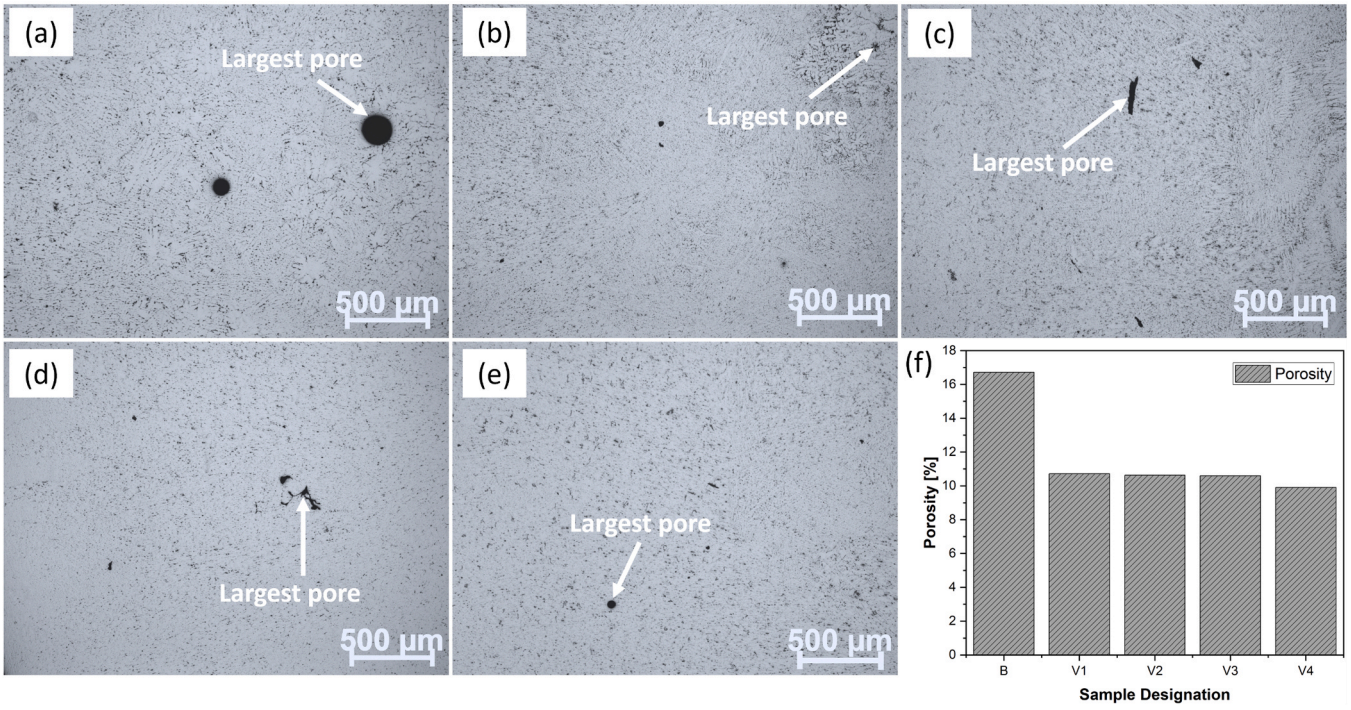

Fig. 5. Specimen porosity (a) optical micrograph of the pores in the base Al-6 %Li alloy without vanadium, (b) optical micrograph of the pores in the specimen containing 0.05 wt %V, (c) optical micrograph of the specimen containing 0.1 wt %V, (d) optical micrograph of the specimen containing 0.5 wt %V, (e) optical micrograph of specimen containing 1.0 wt %V, and (f) comparative summary of the porosity of the specimens.

porosity after the incorporation of 1.0 wt %V.

For a better insight into the pore formation mechanisms, scanning electron microscopy (SEM) analysis was conducted on each specimen (Fig. 6). The base Al-6 %Li alloy exhibited a high level of porosity, primarily attributed to a lack of fusion (LOF) at the center of the cylindrically cast specimen (Fig. 6(a)) due to the evaporation of lithium

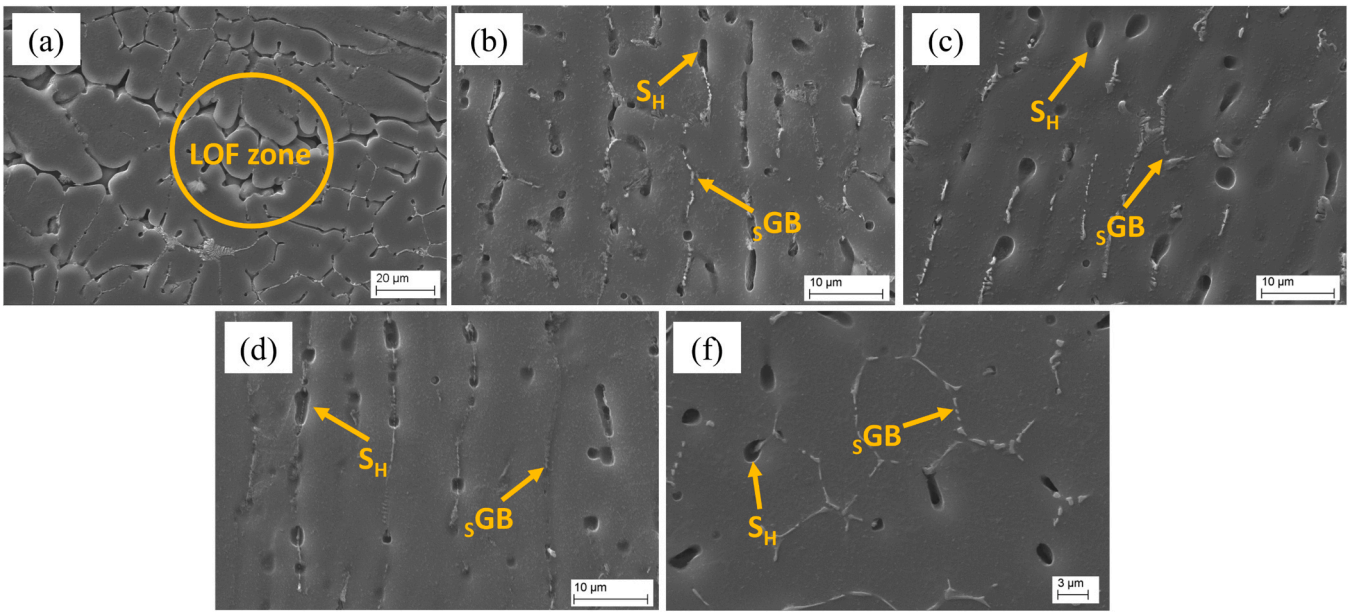

Fig. 6. SEM micrographs of the porous regions of the investigated specimens showing the lack of fusion (LOF) zone, solidification holes (S_H), and grain boundaries with elemental microsegregations ($_sGB$) (a) base Al-6 %Li alloy without vanadium, (b) specimen containing 0.05 wt %V, (c) specimen containing 0.1 wt %V, (d) containing 0.5 wt %V, and (e) specimen containing 1.0 wt %V.

during solidification, resulting in observed pores.

Conversely, in the specimens containing vanadium, the pores were predominantly found at grain boundaries, referred to as solidification holes (S_H), and were more pronounced in the alloy containing 0.05 wt % V (Fig. 6(b)). This trend persisted in the specimens containing 0.1 wt %V (Fig. 6(c)) and 0.5 wt %V (Fig. 6(d)), with the least observed solidifcation holes at grain boundaries in the specimen alloyed with 1.0 wt % V (Fig. 6(e)).

To elucidate the pore formation mechanism, we conducted an investigation on a representative specimen (V4) with a V content of 1.0 wt % and compared it to the base Al-6 %Li alloy (without vanadium) using EDS, as depicted in Fig. 7. Our observations revealed elemental microsegregation, notably iron (Fe), at the grain boundaries. It is worth noting that the aluminum grade A955, employed in the casting process, typically contains Fe at a level not exceeding 0.0015 % as specified by the manufacturer. While analyzing the base alloy through EDS, we observed a low level of Fe at the grain boundaries (Fig. 7(a)). However, upon the introduction of vanadium, the Fe segregation at the grain boundaries increased (Fig. 7(b)). Supplementary Fig. S2 for the sample alloyed with 0.1 wt %V and Fig. S3 for the sample alloyed with 0.5 wt % V further corroborate this observation.

Equipment limitation hindered the observation of Li morphology using the EDS color mapping function. However, at the grain boundary, EDS point analysis results (Table 3) indicates segregation of large contents of Li, approximately 64 wt % and low concentrations of Fe, approximately 2 wt %.

Table 4 provides a comprehensive summary of the corrosion and tribological properties exhibited by the tested specimens. Notably, the

Table 3
Result of energy dispersive X-ray spectroscopy (EDS) point chemical microanalyses at the grain boundary of sample V4, modified with 1 wt % vanadium.

EDS Point	Concentration	Li	Al	Fe	V
GB	Weight %	63.8	36.1	2.0	0.08
	Atom %	83.1	12.7	4.1	0.02

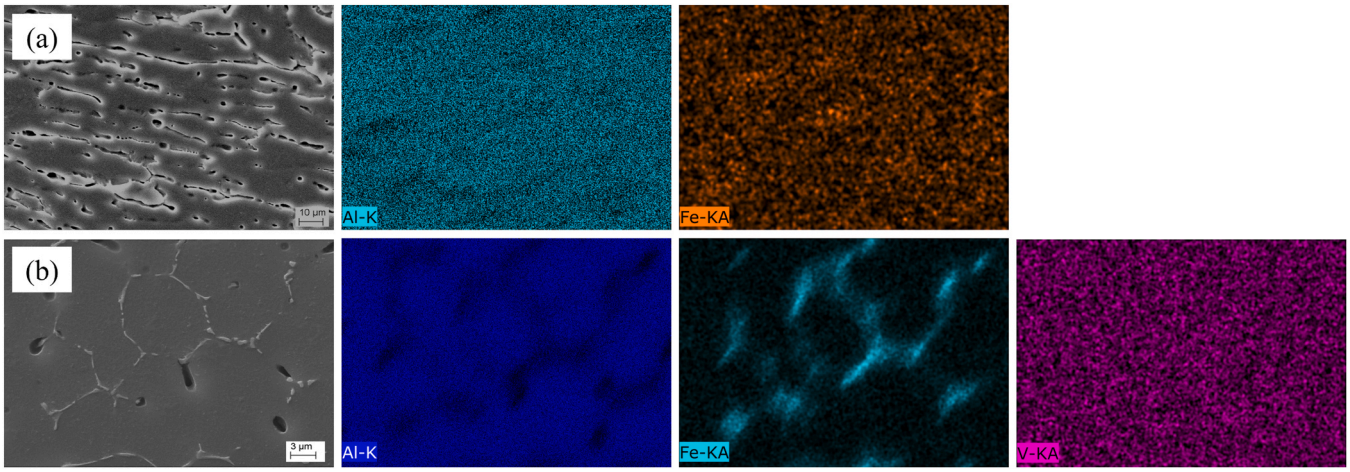

Fig. 7. Energy dispersive X-ray spectroscopy (EDS) maps showing the distribution and segregation of solute atoms in the cast specimens (a) base Al-6 %Li alloy without vanadium, and (b) alloy containing 1.0 wt %V.

Table 4
Summary of corrosion, hardness and tribological properties of investigated specimens.

Sample	E_{ocp} [mV]	E_{corr} [mV]	i_{corr} [μA/cm^2]	Hardness [HV]	Density [g/cm^3]	Wear depth [μm]	Wear rate [10^{-2}m^3/m]
B	-762 ± 75	-736 ± 99	43.6 ± 2.1	51.7±7.3	2.25 ± 0.04	132.2 ± 21.1	3.6±0.50
V1	-789 ± 11	-814 ± 45	11.7 ± 1.0	69.7±3.2	2.42 ± 0.01	151.5 ± 32.2	2.7±0.12
V2	-784 ± 10	-785 ± 26	12.2 ± 1.2	77.6±9.9	2.45 ± 0.03	145.2 ± 28.4	2.5±0.32
V3	-794 ± 18	-776 ± 15	13.8 ± 2.1	55.1±2.5	2.46 ± 0.02	88.2 ± 18.6	2.3±0.10
V4	-781 ± 7	-810 ± 38	3.9 ± 1.0	77.6±4.1	2.48 ± 0.04	51.1 ± 11.7	1.5±0.07

specimen containing 1 wt % vanadium (V4) demonstrated exceptional performance in terms of corrosion resistance, wear resistance, and hardness. This remarkable combination of properties establishes V4 as the optimal specimen for this study, warranting further investigations to gain deeper insights into the influence of vanadium addition on the base alloying from both microstructural and phase evolution perspectives.

3.2. Grain size and phase evolution

Fig. 8(a) and (b) present the EBSD inverse pole figure (IPF) maps for the base Al-6 %Li alloy and the Al-6 %Li modified with 1 wt %V respectively, which exhibit distinct grain orientations depicted by different color maps, as indicated by the unit triangles. The high-angle grain boundaries (HAGBs), represented by green lines, correspond to misorientations exceeding 15 degrees. The red lines denote low-angle grain boundaries (LAGBs) with misorientations ranging from 5 to 15 degrees, while the yellow lines represent low-angle grain boundaries with misorientations ranging from 2 to 5 degrees.

The grain size map in Fig. 8(c) reveals that the base sample consists of large equiaxed grains exhibiting relatively random orientations, with an average grain size of approximately 49 μm (GTA = 2°). Fig. 8(d) illustrates the grain size map of the Al-6 % Li sample modified with 1 wt % vanadium. This map provides evidence of a grain refinement process after the addition of vanadium. The results indicate a 36.7 % reduction in grain size, with an average measured size of approximately 31 μm (GTA = 2°). Fig. 9 shows the number fractions of LAGBs and HAGBs for both specimens. It is observed that the fraction of LAGBs dropped from 19.5 % in the base alloy to 7.0 % after modifying with 1 wt %V. Correspondingly, the HAGs increased from 80.5 % to 93.0 % upon vanadium modification.

Furthermore, a noticeable change in grain morphology is observed. The microstructural morphology evolution, as observed by polarized optical microscopy, in supplementary Fig. S4 reveals a lower occurrence of columnar grains in the base alloy compared to the alloys modified

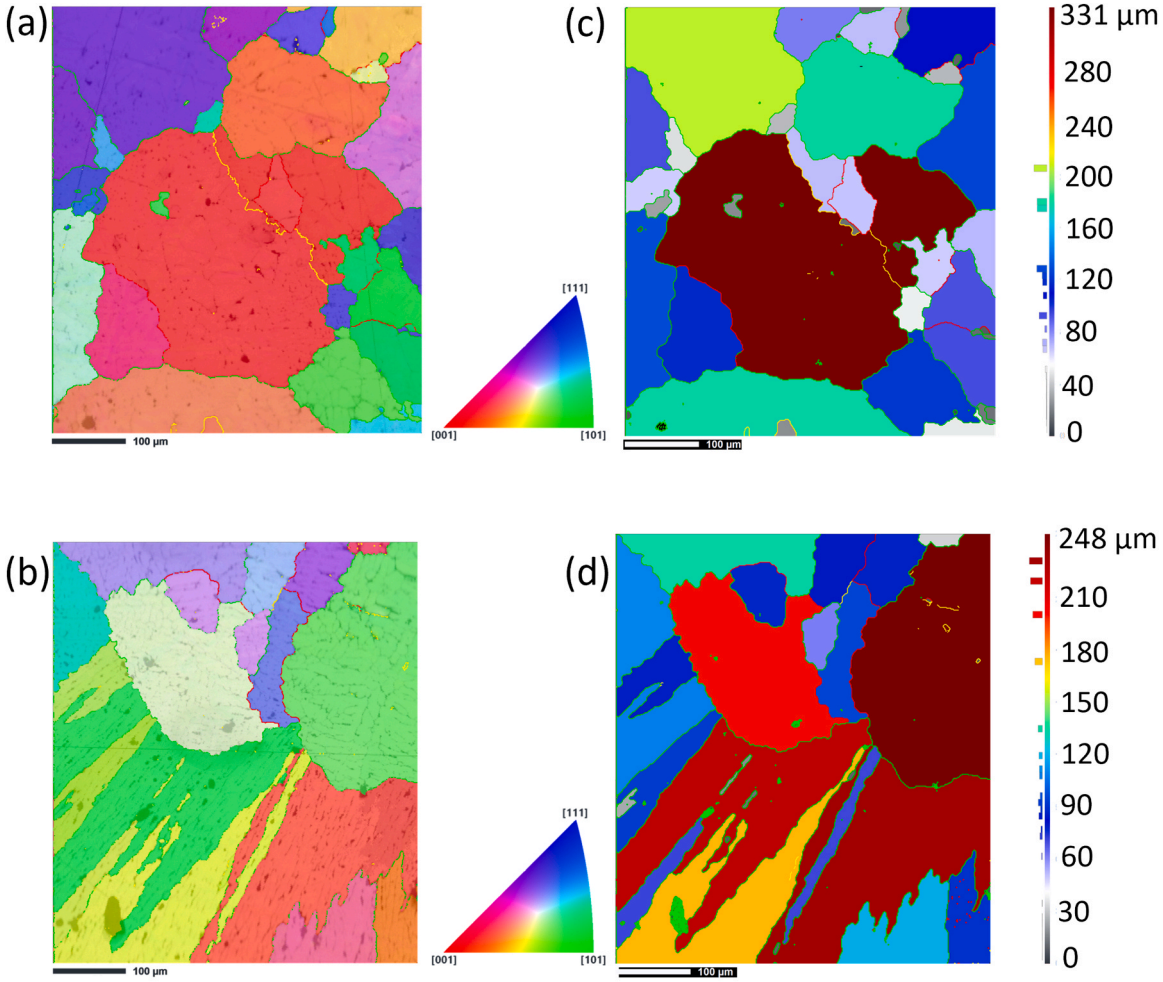

Fig. 8. Microstructure and grain size evolution (a) IPF-Z image of the base alloy, (b) IPF-Z image of the base alloy modified with 1 wt % of vanadium, (c) grain size map of the base alloy (GTA=2°), (d) grain size map of the base alloy modified with 1 wt % of vanadium (GTA = 2°).

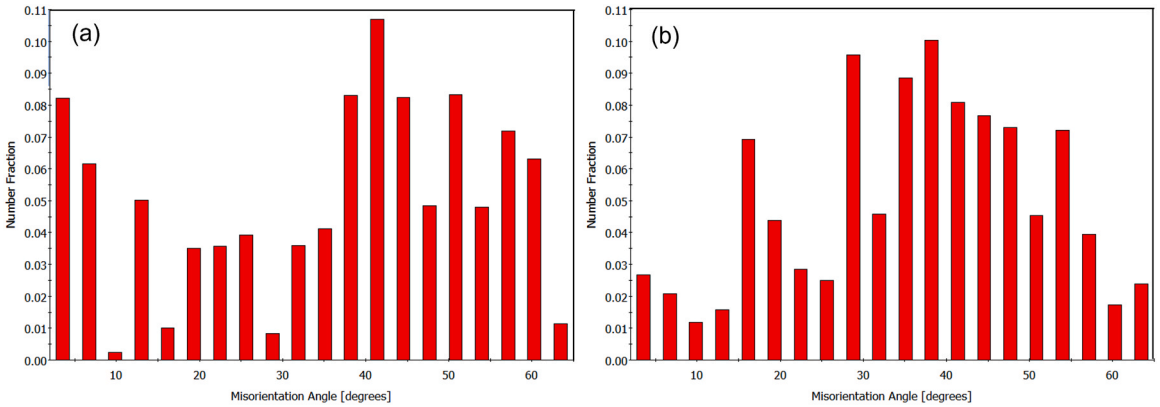

Fig. 9. Electron backscatter diffraction (EBSD) LAGBs and HAGBs misorientation angle number fractions in investigated specimens. (a) base Al6 %Li (b) specimen modified with 1 wt %V.

with vanadium. The microstructures of the base alloy (Fig. 10(a)) and the alloy modified with 1 wt % vanadium (Fig. 10(b)), are characterized by coarse dendritic structures and intergranular non-equilibrium eutectic phases. However, the base alloy exhibits a significantly higher average dendrite arm spacing (DAS) of approximately 35 μm (Fig. 10(c)) compared to the vanadium-alloyed specimen, which has an average DAS of approximately 8 μm (Fig. 10(d)). The DAS sequentially reduced as the V content was gradually increased, as further elaborated by supplementary Fig. S5. This discrepancy is attributed to the grain refinement induced by the presence of vanadium in the modified specimen. The main structural differences are presented in Table 5.

Fig. 11 displays the X-ray diffraction (XRD) patterns illustrating the

Table 5
Structural differences between the base Al-6 %Li alloy and the alloy modified with 1 wt %V.

Specimen	LAGBs	HAGBs	Grain Size	DAS
B	19.5	80.5	49.0	35.0
V4	7.0	93.0	31.0	8.0

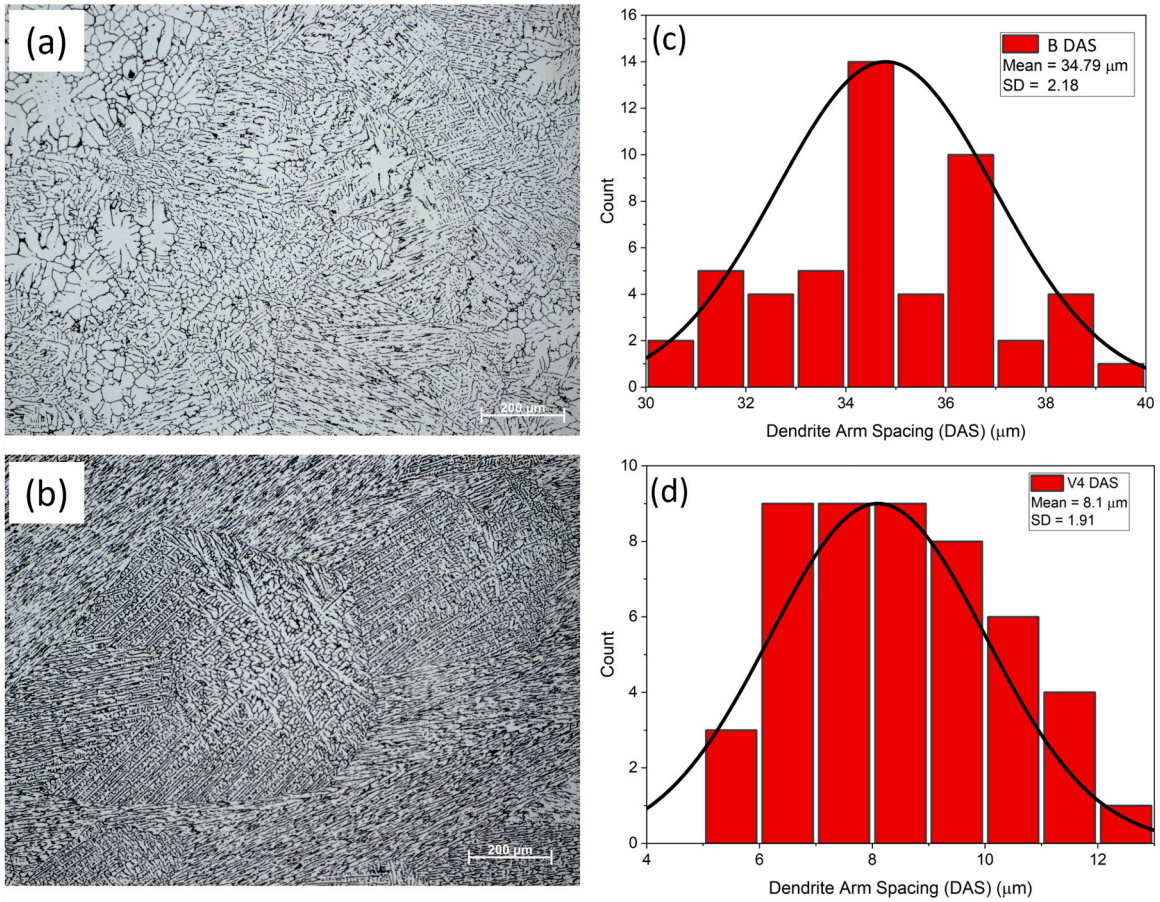

Fig. 10. Optical micrograph of specimens with statistical computation of dendrite arm spacing (DAS) (a) Polarized optical micrograph of the base Al-6 %Li alloy (b) polarized optical micrograph of modified alloy with 1 wt %V (c) DAS distribution plot for base alloy with statistical mean and standard deviation (SD) (d) DAS distribution plot for modified alloy with statistical mean and standard deviation.

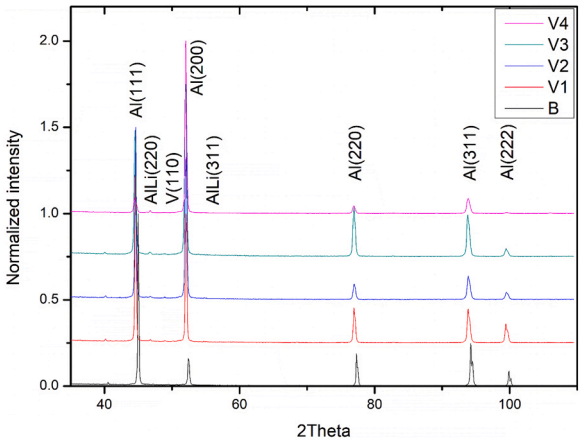

Fig. 11. XRD diffraction pattern of the tested samples.

phase composition of the Al-6 %Li base alloy and specimens containing 0.05 wt %V, 0.1 wt %V, 0.5 wt %V, and 1 wt %V, as a function of vanadium (V) content. The XRD pattern of the base sample exhibits a sharp (111) peak at 2θ ~ 44.9°, along with six relatively weaker peaks - (200) at 2θ ~ 52.3°, (220) at 2θ ~ 77.3°, (311) at 2θ ~ 94.2°, and (222) at 2θ ~ 98.8°, corresponding to the aluminum phase. Additionally, (220) at 2θ ~ 46.8° and (311) at 2θ ~ 54.6° peaks represent the AlLi phase. Moreover, the vanadium-alloyed samples exhibit a minor peak at 2θ ~ 48.9°. It is evident that the inclusion of vanadium leads to a change in the intensity of the Al(200) peak. The sample with the highest vanadium content displays the highest intensity of the Al(200) peak. Two potential reasons account for this intensified peak. First, the addition of vanadium could result in a higher degree of grain refinement. Second, it may cause preferential alignment of the grains (texture development). Supporting this notion, observations from light microscopy and electron backscatter diffraction (EBSD) confirm the development of columnar grains in the modified samples. Furthermore, EBSD analysis was employed to investigate the phase composition of the Al-6 %Li base alloy and the V4 specimens.

Fig. 12 present phase distribution maps obtained from the EBSD analyses using a step size of 0.2 μm at a magnification of 500X. For the base alloy, the EBSD phase analysis verifies the presence of the aluminum phase (blue color, Fig. 12(a)) constituting 88.17 % of the analyzed area, along with the AlLi phase (green color) inhomogenously distributed within the aluminum matrix phase, constituting 11.83 % of the analyzed area. Conversely, the EBSD analysis of the V4 sample, Fig. 12(b), confirms the existence of three distinct phases: 84.47 % aluminum (blue color), 14.67 % AlLi (green color), and 0.86 % vanadium (red color). These results are consistent with the findings derived from the XRD analysis.

Energy dispersive X-ray spectroscopy (EDS) was used to investigate the chemical composition of the interdendritic regions in the cast Al-6 % Li alloy, incorporating 1 wt % vanadium. EDS point analyses were conducted on two distinct locations: the solidified molten pool (P1) and the grain boundary (GB), as shown in Fig. 13 The molten pool exhibited notable concentrations of Al (74.86 wt %) and Li (25.03 wt %), along with the presence of vanadium. Conversely, the grain boundary demonstrated a segregation of Li (61.80 wt %), Fe (2.02 %) and Al (36.10 wt %). This observation indicates the dispersion of Li within the Al matrix throughout the interdendritic phases, further corroborating the previous identification of the AlLi phase through EBSD and XRD analyses. EDS results are summarized in Table 6.

4. Discussion

The introduction of lithium into Al-based alloys induces microstructural alterations and heightens the susceptibility of the resulting alloy to exfoliation corrosion. The microstructure, encompassing the quantity, dimensions, distribution, and chemical composition of precipitated phases, stands as a paramount determinant influencing the corrosion propensities of Al-based alloys [42,43]. Lithium, by nature, exhibits pronounced chemical reactivity [34,44]. Elevated concentrations of lithium in Al-based alloys foster the formation of δ (AlLi) precipitates, which are highly reactive phases found within the molten pool matrix and grain boundary regions [45]. The δ phase is a key factor governing the formation of intermetallic compounds, such as Al_4Li_3, Al_4Li_9, and Al_3Li, within the binary Al-Li alloy system. Previous studies by Okamoto [46] have established that the metastable Al_3Li compound predominates when lithium content remains below 10 wt % in the Al-Li binary system. Whiles Tao et. al [47] have shown that artificial aging has a strong tendency to precipitate the Al_3Li phase, additional research conducted by Liu et al. [48] suggests that natural ageing at room temperature can also facilitate the formation of the Al_3Li intermetallic and

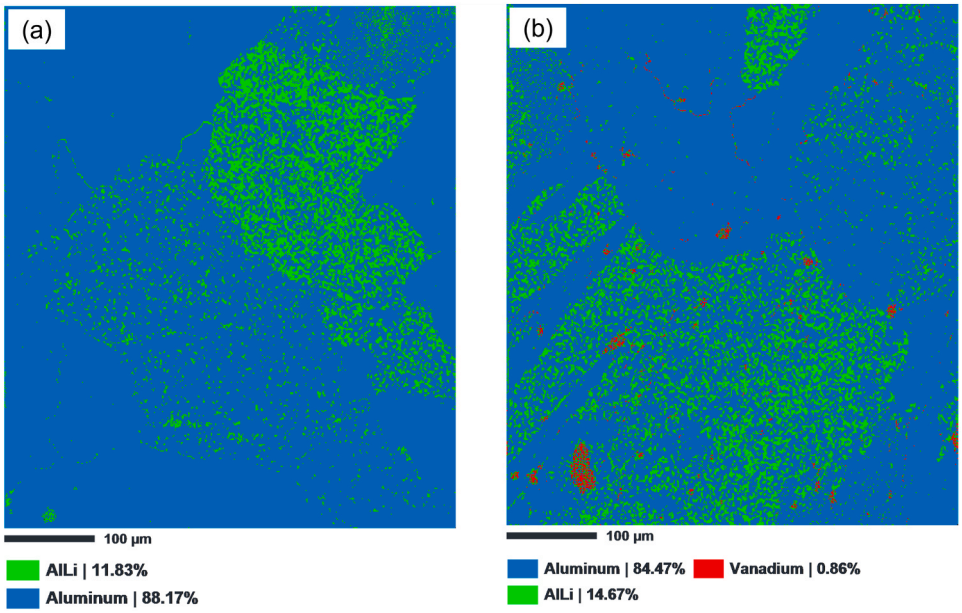

Fig. 12. EBSD phase distribution maps (a) base Al-6 %Li alloy, and (b) base Al-6 %Li alloy modified with 1 % of vanadium, respectively.

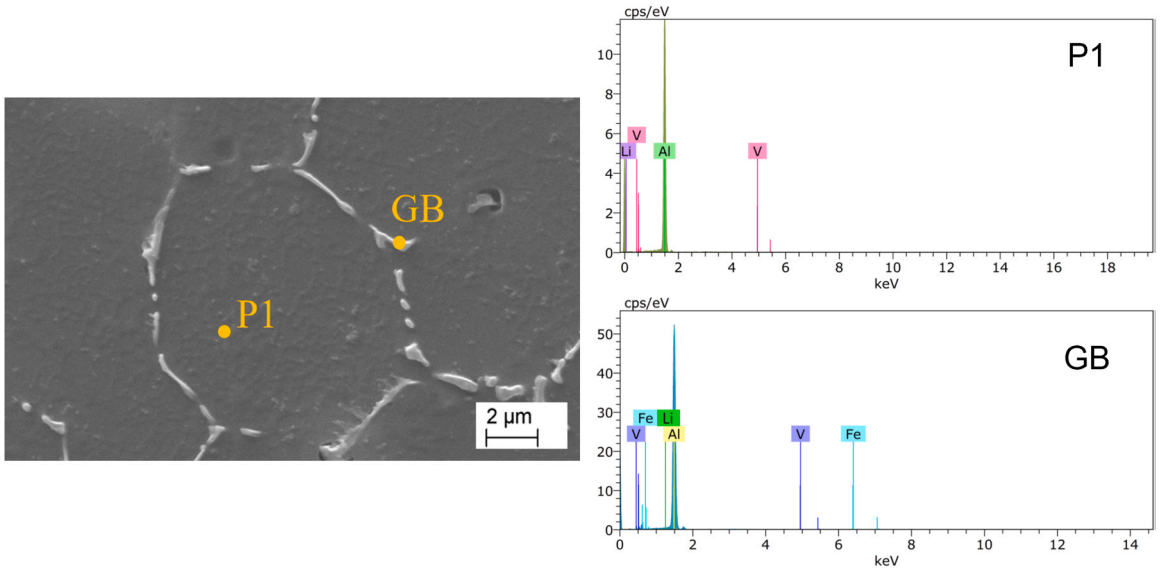

Fig. 13. SEM microstructure of base Al-6 %Li alloy modified with 1 wt %V showing grain boundaries and points in the molten pool (P1) and on the grain boundary (GB) subjected to energy dispersive X-ray spectroscopy (EDS) chemical analyses.

Table 6
Result of energy dispersive X-ray spectroscopy (EDS) point chemical microanalyses.

EDS Point	Concentration	Li	Al	Fe	V
P1	Weight %	25.0	74.9	–	0.11
	Atom %	56.5	43.6	–	0.03
GB	Weight %	63.8	36.1	2.0	0.08
	Atom %	83.1	12.7	4.1	0.02

Guinier-Preston (GP) zones. Niskanen et al. [45] underscored the reactivity of the δ phase through the preferential leaching of many grain boundary precipitates during electropolishing. Thus, when δ becomes the prevailing microstructural feature, one can observe a notable anodic shift in the corrosion behaviour of Al-Li alloys. It is crucial to note that the corrosion resistance of Al-Li alloys diminishes rapidly following age-processing techniques such as rapid solidification. In this context, higher values of corrosion current densities have been documented for samples in their initial states. Notably, as indicated in the literature [23, 49,50], the addition of vanadium to Al-based alloys engenders a commendable synergy between corrosion resistance and mechanical properties, encompassing hardness and wear characteristics. Esteves et al. [35] substantiated the beneficial influence of vanadium on the corrosion behavior of AA5083 alloy, evident through elevated corrosion and repassivation potentials. The enhanced corrosion performance of Al-V alloys can be attributed to the expanded solid solubility of vanadium, resulting in the formation of V-ions within corrosion pits. Additionally, vanadium is deposited onto cathodic particles, subsequently diminishing their capacity to sustain cathodic currents. Ozdemir et al. [23] have demonstrated a twofold increase in the hardness of 2024 alloy with the incorporation of vanadium, primarily attributable to solid solution strengthening and dispersion hardening induced by vanadium. Elevated hardness, in turn, augments tribological properties, a phenomenon underscored in our study and corroborated by the investigations presented by Kumar et al. [50].

The observed trend in the hardness of the alloys after vanadium modification aligns seamlessly with the outcomes of previous research, which have consistently reported elevated hardness levels in alloys after the introduction of vanadium [49,51–53]. Furthermore, these studies have systematically documented a substantial refinement in grain structure upon vanadium alloying. The underlying mechanism responsible for this grain refinement effect can be attributed to the well-established Hall-Petch relationship, Eq. (7) [54].

$$\sigma_y = \sigma_i + kd^{-\frac{1}{2}} \tag{7}$$

Where σ_y is the yield strength, σ_i is the lattice dislocation movement resistance, k is the grain boundary locking term for measuring the relative hardening contribution by grain boundaries, and d is the diameter of grain. In the context of hardness, the Hall-Petch relationship posits that the hardness of a material tends to increase proportionally with the refinement of its grain structure. This phenomenon arises from the greater number of grain boundaries in materials with smaller grains, which actively serve as barriers to dislocations, thereby contributing to strengthening the mechanical properties, including hardness. As such, the observed hardness improvements in our investigated alloys following vanadium incorporation can be rationalized by the notable grain refinement induced by the presence of vanadium.

However, the influence of grain refinement on the corrosion resistance of aluminum alloys has become a subject of considerable attention in recent investigations, and yet poorly understood. In a notable study, Moustafa et al. [55] delved into the impact of grain refinement, achieved through the addition of TiB, on the corrosion resistance of 5052 aluminum alloy. They reported an evident increase in corrosion resistance directly associated with the process of grain size refinement. However, contrasting findings were reported by Orłowska et al. [56] concerning commercially pure aluminum. Their investigations encompassed variations in grain size, shape, and the fraction of high-angle grain boundaries (HAGBs), yet no significant difference in corrosion behavior was observed. However, noteworthy distinctions in corrosion pits were detected, suggesting a subtle influence of grain size on localized corrosion processes. Additionally, Tian et al. [57] conducted a comprehensive study on a naturally aged bimodal AA7075 aluminum alloy, revealing a positive correlation between increased ratios of fine grains and heightened pitting corrosion resistance. This relationship was manifested through a higher frequency of pitting current transients, indicating an overall improvement in pitting corrosion resistance. In the context of our own investigation, we focused on vanadium alloying as a means to induce significant grain refinement in the aluminum alloy. This microstructural transformation was evident in playing a key role in enhancing both corrosion resistance and tribological properties. These findings align consistently with prior research that have highlighted a direct association between grain refinement and corrosion and wear

resistance in different structural alloys. For instance, in a recent investigation conducted by Ji et. al [58], an exploration into the interplay between grain refinement and corrosion resistance was undertaken. The study focused on single α-phase Ti-Zr-based alloys, and notable advancements in corrosion resistance were observed following the grain refinement process. Specifically, the grain refinement procedure was found to improve the stability of the passivation film as well as actively inhibit the appearance of corrosion pits inside the grains. This outcome aligns with the earlier findings reported by Jinlong [59], where a substantial enhancement in corrosion resistance was ascribed to grain refinement in the case of Ni-based alloy 690. Also, Akbarpour et al. [60] achieved grain refinement in a nanostructured Al-SiC nanocomposite, with 4 % SiC additions, leading to a remarkable increase in wear resistance. This improvement was attributed to the synergistic effects of grain size refinement and the presence of nanoparticles in the alloy. Our investigations underscore the critical influence of grain size on the wear and corrosion resistance of aluminum-lithium alloys. By employing vanadium alloying to facilitate substantial grain refinement, we observed an effective contribution to enhancing the corrosion resistance and tribological properties of the alloy with this approach.

Nonetheless, the phenomenon of reduced porosity in the modified specimens can be attributed to the non-equilibrium segregation of solute elements at the grain boundaries. In this context, vacancy-solute complexes are formed resulting from a peritectic reaction Fe + Al21V2 ↔ (Al) [61]. This is as a result of the solubility of V in Al being 0.91 at % at 735 ℃, 0.2 at % at 660 ℃, and 0.11 at % at 500 ℃. Consequently, the occurrence of the peritectic reaction, leading to the formation of vacancy-solute complexes containing Fe, can be traced back to the cooling process of the cast specimens from 750 ℃ to room temperature. Zhang et al. [62] have postulated that two major conditions which underscore the formation of porosity in Al-li alloys are pressure and cooling rate. In our study, the large temperature range for the cooling process hampers the establishment of true equilibrium concentrations for the vacancy-solute complexes, except at vacancy sinks. Consequently, a vacancy concentration gradient develops in the cooled melt, facilitating the movement of vacancies towards these sinks, where solute atoms are deposited. The non-equilibrium segregation at the grain boundaries, as evidenced through EDS mapping (Fig. 6(b)), arises from the accumulation of excess solute atoms at these locations, as well as the accumulation of complexes at the vacancy sinks increases with higher vanadium content. Through ab initio calculations, Wang et al. [63] have successfully demonstrated a strong binding effects of Li atoms to vacancies in the Al-Li-vacancy complex structures, using an Al-Li binary alloy containing 4 wt %Li. Furthermore, they discovered that vacancies situated in distinct sub-lattices manifest short- and long-range effects, specifically designed to influence the bonding strength of the constituent atoms. This cumulative complex effectively impedes the evaporation of Li during the solidification of the melt, providing a compelling rationale for the observed decline in porosity as the vanadium concentrations in the specimen increase. [64,65].

5. Conclusions

- This study investigated the effects of vanadium alloying on the structure, corrosion and tribological performance of an Al-6 %Li alloy, considering varying V contents: 0.05 wt %, 0.1 wt %, 0.5 wt %, and 1.0 wt %.
- The findings demonstrate that the addition of 1.0 wt % vanadium is optimal for enhancing the corrosion resistance and wear resistance of the alloy. Notably, the wear rate decreased from $3.6 \pm 0.50 \times 10^{-2}$ m^3/m to $1.5 \pm 0.07 \times 10^{-2}$ m^3/m, the hardness increased from 51.7 ± 7.3 HV to 77.6 ± 4.1 HV, and the corrosion current density decreased from 43.6 μA/cm^2 to 3.9 μA/cm^2 upon incorporating 1 wt % V into the alloy, all while keeping the density low at 2.48 g/cm^3.
- The incorporation of vanadium into the alloy led to a notable decrease in its overall porosity. This reduction can be attributed to a peritectic reaction occurring among the constituents Fe, Al, and V, which subsequently resulted in the generation of vacancy-solute complexes along the grain boundaries.
- Employing electron backscatter diffraction (EBSD) coupled with optical microscopy, significant grain refinement was observed in the alloy when vanadium was added. The average grain size reduced by 36.7 % from 49 μm to 31 μm, and the dendrite arm spacing (DAS) in the microstructure decreased from 35 μm to 8 μm.
- Phase and chemical composition analyses confirmed the formation and presence of δ (AlLi) phase within the interdendritic regions. Notably, this phase fosters the formation of Al_3Li intermetallic which was more pronounced and intensified with the addition of 1 wt % V. This phenomenon significantly contributed to the observed improvements in the corrosion resistance and tribological properties of the vanadium-modified alloy.

CRediT authorship contribution statement

Conceptualization – M.A, S.A.N, I.N.G, G.F.B, A.N.S.A; Data curation – A.N.S.A, A.W, P.M.N, K.M, P.S; Formal analysis – A.N.S.A, A.W, P.S; Investigation – A.N.S.A, A.W, K.M, P.S, P.M.N; Methodology – A.N.S.A, S.A.N, I.N.G, A.W, M.A; Resources – M.A, S.A.N, I.N.G, G.F.B; Supervision – M.A, G.F.B; Writing - original draft – A.N.S.A, A.W, P.S; Writing - review & editing – S.A.N, I.N.G, G.F.B, A.N.S.A, P.S, A.W, M.A, K.M.

All authors have read and agreed to the final version of this paper.

Declaration of Competing Interest

The authors declare that they have no known competing financial interests or personal relationships that could have appeared to influence the work reported in this paper.

Data Availability

Data will be made available on request.

Acknowledgments

The authors would like to show appreciation to the Silesian University of Technology with support through the Excellence Initiative – Research University project number 32/014/SDU/10–22-24 and 10/100/BKM_23/0060.

Appendix A. Supporting information

Supplementary data associated with this article can be found in the online version at doi:10.1016/j.jallcom.2023.172910.

References

[1] X. Ding, et al., Effect of large pre-deformation on microstructure and mechanical properties of 7B52 laminated aluminum alloy, J. Alloy. Compd. 967 (2023), 171749, https://doi.org/10.1016/j.jallcom.2023.171749.
[2] K. Lee, et al., Genetic design of new aluminum alloys to overcome strength-ductility trade-off dilemma, J. Alloy. Compd. 947 (2023), 169546, https://doi.org/10.1016/j.jallcom.2023.169546.
[3] P. Snopiński, A.N.S. Appiah, O. Hilšer, M. Kotoul, Investigation of microstructure and mechanical properties of SLM-fabricated AlSi10Mg alloy post-processed using equal channel angular pressing (ECAP), Materials 15 (22) (2022) 7940.
[4] W. Han, X. Hu, Corrosion of Al-Li alloy melt on oxide refractories, Anti-Corros. Methods Mater. (2023).
[5] M. Qi, et al., Superior mechanical properties and microstructural evolution of powder metallurgy 2195 Al-Li alloy subjected to hot extrusion, J. Alloy. Compd. 962 (2023), 171184, https://doi.org/10.1016/j.jallcom.2023.171184.
[6] D. Lu, et al., Effect of grain structure on fatigue crack propagation behavior of Al-Cu-Li alloys, J. Mater. Sci. Technol. 148 (2023) 75–89, https://doi.org/10.1016/j.jmst.2022.10.085.
[7] F. Abdi, H. Aghajani, A. Taghizadeh Tabrizi, L. Nasimi, F. Fazli Shokouhi, Study on the effect of the crack closing of AlCoCrFeMnNi high entropy alloy electro-spark deposited coating by plasma nitriding on the corrosion resistance, J. Alloy. Compd. 966 (2023), 171629, https://doi.org/10.1016/j.jallcom.2023.171629.

[8] C. Zhang, W. Lu, Unveiling contribution of overload-induced residual stress to fatigue retardation pertinent to crack closure and stress intensity, Mater. Sci. Eng. A vol. 831 (2022), 142268.

[9] B. Yang, et al., Improving corrosion resistance of anodized AA2099-T83 Al-Cu-Li alloy through post-treatment in a lithium nitrate-based solution, Surf. Coat. Technol. 441 (2022), 128501, https://doi.org/10.1016/j.surfcoat.2022.128501.

[10] X. Xu, G. Zhao, S. Yu, Y. Wang, X. Chen, W. Zhang, Effects of extrusion parameters and post-heat treatments on microstructures and mechanical properties of extrusion weld seams in 2195 Al-Li alloy profiles, J. Mater. Res. Technol. 9 (3) (2020) 2662–2678, https://doi.org/10.1016/j.jmrt.2019.12.095.

[11] Y. Li, et al., Microstructural evolution and properties of electromagnetic cast-rolled novel Al–Li alloy under different heat treatment procedures, J. Mater. Res. Technol. 16 (2022) 864–878, https://doi.org/10.1016/j.jmrt.2021.12.036.

[12] Y. Wang, et al., A comparative study on precipitation behavior of a sand-cast Al–Li–Cu alloy with the different quenching rates, J. Mater. Res. Technol. 21 (2022) 4893–4907, https://doi.org/10.1016/j.jmrt.2022.11.079.

[13] S.-X. Deng, et al., Effect of Zr addition on the microstructure evolution and mechanical properties of extruded Al-Cu-Li-Mn alloys, Mater. Charact. 202 (2023), 113011, https://doi.org/10.1016/j.matchar.2023.113011.

[14] E.A. Hajjioui, K. Bouchaâla, M. Faqir, E. Essadiqi, A review of manufacturing processes, mechanical properties and precipitations for aluminum lithium alloys used in aeronautic applications, Heliyon 9 (3) (2023), e12565, https://doi.org/10.1016/j.heliyon.2022.e12565.

[15] X. Kong, T.F. Morgeneyer, D. Missoum-Benziane, G. Rousselier, A polycrystalline damage model applied to an anisotropic aluminum alloy 2198 under non-proportional load path changes, Int. J. Plast. 168 (2023), 103674, https://doi.org/10.1016/j.ijplas.2023.103674.

[16] Y. Li, G. Xu, G. Guo, S. Liu, X. Peng, Study on fatigue crack propagation behavior of 2050 AlLi alloy during non-isothermal aging, Mater. Charact. (2023), 113170, https://doi.org/10.1016/j.matchar.2023.113170.

[17] C. Shyamlal, et al., Corrosion behavior of friction stir Welded AA8090-T87 aluminum alloy, Materials 15 (15) (2022) 5165.

[18] A.S. Khan, V.J. Badheka, A.B. Chaudhari, V.S. Gadakh, Experimental investigation of friction stir welding of aluminum alloy AA8090-T3 using taguchi method, J. Mater. Eng. Perform. 32 (11) (2023) 4787–4795.

[19] A. Kalaiyarasan, S. Sundaram, K. Gunasekaran, Tribological characteristics of AA8090-WC-ZrC metal matrix composites prepared by stir casting process for aerospace applications, Ind. Lubr. Tribol. 73 (6) (2021) 980–985.

[20] C. Shyamlal, S. Rajesh, J.W. Jappes, M. Ravichandran, S. Abuthakeer, Effects of friction stir welding process on the microstructure and mechanical properties of AA8090—T87 aluminium alloy, Surf. Topogr. Metrol. Prop. 10 (4) (2022), 045029.

[21] C. Wang, et al., Thermodynamic description of the binary Al–V and ternary Al–Cr–V systems, Calphad 82 (2023), 102579, https://doi.org/10.1016/j.calphad.2023.102579.

[22] A. Sahli, et al., Effect of an addition of vanadium on the mechanical properties of the A6061 alloy deformed by accumulative roll bonding, J. Mater. Eng. Perform. 30 (10) (2021) 7510–7522.

[23] F. Ozdemir, R.K. Gupta, Influence of vanadium addition on corrosion behavior of high-energy ball milled aluminum alloy 2024, Mater. Corros. 74 (2) (2023) 285–292.

[24] Y. Sun, F. Zhang, J. Ren, G. Song, Effect of Li content on the microstructure and mechanical properties of as-homogenized Mg-Li-Al-Zn-Zr Alloys, Alloys 2 (2) (2023) 89–99.

[25] M. Adamiak, A.N.S. Appiah, A. Woźniak, P.M. Nuckowski, S.A. Nazarov, I. N. Ganiev, Impact of titanium addition on microstructure, corrosion resistance, and hardness of As-Cast Al+ 6% Li alloy, Materials 16 (7) (2023) 2671.

[26] C. Li, Y. He, H. Huang, Effect of lithium content on the mechanical and corrosion behaviors of HCP binary Mg–Li alloys, J. Magnes. Alloy. 9 (2) (2021) 569–580, https://doi.org/10.1016/j.jma.2020.02.022.

[27] R. Babilas, et al., Influence of Fe, Cr, and Cu addition on the microstructure, hardness, and anticorrosion properties of Al–Ni–Y alloys, Arch. Civ. Mech. Eng. 22 (2) (2022) 1–15, https://doi.org/10.1007/S43452-022-00404-W/FIGURES/11.

[28] H. Yan, K. Dejun, Effects of Cr and Ta additions on microstructure, corrosion-wear and electrochemical performances of laser cladded Fe90-Al2O3 coating in 3.5% NaCl solution, Anti-Corros. Methods Mater. 69 (4) (2022) 442–451.

[29] K.L. Johnson, Contact mechanics and the wear of metals, Wear 190 (2) (1995) 162–170, https://doi.org/10.1016/0043-1648(95)06665-9.

[30] B. Noble, S.J. Harris, K. Dinsdale, The elastic modulus of aluminium-lithium alloys, J. Mater. Sci. 17 (2) (1982) 461–468, https://doi.org/10.1007/BF00591481/METRICS.

[31] J. Sekyi-Ansah, et al., Surface characteristics and cavitation damage in 8090Al–Li alloy by using cavitation water jet peening processing, Iran. J. Sci. Technol. - Trans. Mech. Eng. 45 (1) (2021) 299–309, https://doi.org/10.1007/S40997-020-00401-5.

[32] P. Zhang, et al., Dry fretting and sliding wear behavior of 7075-T651 aluminum alloy under linear reciprocating motion: a comparative study, Wear 526–527 (2023), 204942, https://doi.org/10.1016/J.WEAR.2023.204942.

[33] S.L. Yee, H. Wan, M. Chen, L. Li, J. Li, X. Ma, Development of a cleaner route for aluminum–vanadium alloy production, J. Mater. Res. Technol. 16 (2022) 187–193, https://doi.org/10.1016/J.JMRT.2021.11.125.

[34] X. Chen, X. Ma, G. Zhao, Y. Wang, X. Xu, Effects of re-solution and re-aging treatment on mechanical property, corrosion resistance and electrochemical behavior of 2196 Al-Cu-Li alloy, Mater. Des. 204 (2021), 109662, https://doi.org/10.1016/j.matdes.2021.109662.

[35] L. Esteves, et al., Effect of V content on corrosion behavior of high-energy ball milled AA5083, Corros. Sci. 186 (2021), 109465, https://doi.org/10.1016/j.corsci.2021.109465.

[36] M. Suresh, R. Kalsar, A.M. More, A. Bisht, N. Nayan, S. Suwas, Evolution of microstructure and texture in the third generation Al–Li alloy AA2195 during warm hybrid processing, J. Alloy. Compd. 855 (2021), 156750, https://doi.org/10.1016/j.jallcom.2020.156750.

[37] S. Kumar, J.K. Katiyar, G.S. Kesharwani, B.S. Roy, Microstructure, mechanical, and force-torque generation properties of friction stir welded third generation Al/Li alloy at higher traverse speed, Mater. Today Commun. 35 (2023), 106084, https://doi.org/10.1016/j.mtcomm.2023.106084.

[38] R. Ambat, A.J. Davenport, G.M. Scamans, A. Afseth, Effect of iron-containing intermetallic particles on the corrosion behaviour of aluminium, Corros. Sci. 48 (11) (2006) 3455–3471, https://doi.org/10.1016/j.corsci.2006.01.005.

[39] G. Frankel, Pitting corrosion of metals: a review of the critical factors, J. Electrochem. Soc. 145 (6) (1998) 2186.

[40] M. Iannuzzi, G.S. Frankel, Mechanisms of corrosion inhibition of AA2024-T3 by vanadates, Corros. Sci. 49 (5) (2007) 2371–2391, https://doi.org/10.1016/j.corsci.2006.10.027.

[41] C. Witharamage, J. Christudasjustus, J. Smith, W. Gao, R. Gupta, Corrosion behavior of an in situ consolidated nanocrystalline Al-V alloy, NPJ Mater. Degrad. 6 (1) (2022), 15.

[42] M. Guérin, et al., Identification of the metallurgical parameters explaining the corrosion susceptibility in a 2050 aluminium alloy, Corros. Sci. 102 (2016) 291–300, https://doi.org/10.1016/j.corsci.2015.10.020.

[43] X. Lei, et al., Studies on pitting corrosion of Al-Cu-Li alloys part I: effect of li addition by microstructural, electrochemical, in-situ, and pit depth analysis, Materials 12 (10) (2019) 1600.

[44] X. Zheng, H. Yin, Y. Shu, Z. Chu, Z. Liu, The corrosion behavior and tensile strength of the 2060 Al-Li alloy with different heat treatments, Front. Mater. 9 (2022) 1003204.

[45] P. Niskanen, T.H. Sanders, J.G. Rinker, M. Marek, Corrosion of aluminum alloys containing lithium, Corros. Sci. 22 (4) (1982) 283–304, https://doi.org/10.1016/0010-938X(82)90031-2.

[46] H. Okamoto, Al-Li (Aluminum-Lithium), J. Phase Equilibria Diffus. 33 (2012) 500–501.

[47] Y. Tao, Z. Zhang, P. Xue, D.R. Ni, B.L. Xiao, Z.Y. Ma, Effect of post weld artificial aging and water cooling on microstructure and mechanical properties of friction stir welded 2198-T8 Al-Li joints, J. Mater. Sci. Technol. 123 (2022) 92–112, https://doi.org/10.1016/j.jmst.2022.01.020.

[48] Z. Liu, et al., Effect of filler wire on mechanical properties, microstructure and natural aging behavior of 2A55 Al-Li Alloy TIG welded joint, Metals 13 (2) (2023) 347.

[49] S. Boczkal, M. Lech-Grega, J. Morgiel, K. Piela, Effect of vanadium additions on the structure of aluminium (Al99. 5) and 6xxx aluminium alloys, Light Met. 2014 (2016) 261–264.

[50] A. Kumar, C. Sasikumar, Effect of Vanadium addition to Al-Si alloy on its mechanical, tribological and microstructure properties (Part A), 5th Int. Conf. Mater. Process. Charact. ICMPC 2016 4 (2) (2017) 307–313, https://doi.org/10.1016/j.matpr.2017.01.026.

[51] W. Zhou, et al., The effect of vanadium on the microstructure and mechanical properties of TiAl alloy fabricated by twin-wire directed energy deposition-arc, Addit. Manuf. 62 (2023), 103382, https://doi.org/10.1016/j.addma.2022.103382.

[52] R. Wang, et al., The effect of RRA treatment on mechanical properties and wear behavior in vanadium micro-alloyed Hadfield steel, J. Mater. Res. Technol. 24 (2023) 9884–9896, https://doi.org/10.1016/j.jmrt.2023.05.156.

[53] D. Hu, Z. Li, H. Chen, Y. Liu, Q. Fang, W. Long, Effect of vanadium addition on the microstructure and properties of NiCuBSi-WC60 composite coatings deposited by laser direct deposition, Mater. Charact. 199 (2023), 112746, https://doi.org/10.1016/j.matchar.2023.112746.

[54] R.B. Figueiredo, M. Kawasaki, T.G. Langdon, Seventy years of Hall-Petch, ninety years of superplasticity and a generalized approach to the effect of grain size on flow stress, Prog. Mater. Sci. (2023), 101131.

[55] E.B. Moustafa, A.O. Mosleh, Effect of (Ti–B) modifier elements and FSP on 5052 aluminum alloyλ, J. Alloy. Compd. 823 (2020), 153745 https://doi.org/10.1016/j.jallcom.2020.153745.

[56] M. Orłowska, E. Ura-Bińczyk, L. Olejnik, M. Lewandowska, The effect of grain size and grain boundary misorientation on the corrosion resistance of commercially pure aluminium, Corros. Sci. 148 (2019) 57–70, https://doi.org/10.1016/j.corsci.2018.11.035.

[57] W. Tian, S. Li, B. Wang, J. Liu, M. Yu, Pitting corrosion of naturally aged AA 7075 aluminum alloys with bimodal grain size, Corros. Sci. 113 (2016) 1–16, https://doi.org/10.1016/j.corsci.2016.09.013.

[58] P. Ji, et al., Synergistic effect of Zr addition and grain refinement on corrosion resistance and pitting corrosion behavior of single α-phase Ti-Zr-based alloys, J. Alloy. Compd. 896 (2022), 163013, https://doi.org/10.1016/j.jallcom.2021.163013.

[59] J. Lv, Effect of grain size on mechanical property and corrosion resistance of the Ni-based alloy 690, J. Mater. Sci. Technol. 34 (9) (2018) 1685–1691, https://doi.org/10.1016/j.jmst.2017.12.017.

[60] M. Akbarpour, S. Alipour, Microstructure and tribological properties of nanostructured aluminum reinforced with SiC nanoparticles fabricated by powder metallurgy route, Trans. Indian Inst. Met. 71 (3) (2018) 745–752.

[61] Y. Lin, Z. Zheng, S. Li, X. Kong, Y. Han, Microstructures and properties of 2099 Al-Li alloy, Mater. Charact. 84 (2013) 88–99, https://doi.org/10.1016/j.matchar.2013.07.015.

[62] Y. Zhang, et al., Uncovering the effects of local pressure and cooling rates on porosity formation in AA2060 Al-Li alloy, Mater. Today Commun. 35 (2023), 106384, https://doi.org/10.1016/j.mtcomm.2023.106384.
[63] S. Wang, J. Wang, C. Zhang, C. Xue, Continuous precipitate modes of the δ′-Al3Li phase in Al-Li alloys, J. Alloy. Compd. 904 (2022), 163800, https://doi.org/10.1016/j.jallcom.2022.163800.
[64] Y. Yao, D. Wu, X. Zhao, F. Yang, Premature failure induced by non-equilibrium grain-boundary tantalum segregation in air-plasma sprayed ZrO2− YO1. 5− TaO2. 5 thermal barrier coatings, Int. J. Miner. Metall. Mater. 29 (12) (2022) 2189–2200.
[65] T. Kawakubo, K. Ushioda, H. Fujii, Grain boundary segregation and toughness of friction-stir-welded high-phosphorus weathering steel, Mater. Sci. Eng. A 832 (2022), 142350.